



Electrochemically Induced Phase Transition in $V_3O_7 \cdot H_2O$ Nanobelts/Reduced Graphene Oxide Composites for Aqueous Zinc-Ion Batteries

Cao, Huili; Zheng, Zhiyong; Norby, Poul; Xiao, Xinxin; Mossin, Susanne

Published in:
Small

Link to article, DOI:
[10.1002/smll.202100558](https://doi.org/10.1002/smll.202100558)

Publication date:
2021

Document Version
Peer reviewed version

[Link back to DTU Orbit](#)

Citation (APA):

Cao, H., Zheng, Z., Norby, P., Xiao, X., & Mossin, S. (2021). Electrochemically Induced Phase Transition in $V_3O_7 \cdot H_2O$ Nanobelts/Reduced Graphene Oxide Composites for Aqueous Zinc-Ion Batteries. *Small*, 17(24), Article e2100558. <https://doi.org/10.1002/smll.202100558>

General rights

Copyright and moral rights for the publications made accessible in the public portal are retained by the authors and/or other copyright owners and it is a condition of accessing publications that users recognise and abide by the legal requirements associated with these rights.

- Users may download and print one copy of any publication from the public portal for the purpose of private study or research.
- You may not further distribute the material or use it for any profit-making activity or commercial gain
- You may freely distribute the URL identifying the publication in the public portal

If you believe that this document breaches copyright please contact us providing details, and we will remove access to the work immediately and investigate your claim.

Cite this paper: <https://doi.org/10.1002/sml.202100558>

Electrochemically induced phase transition in $V_3O_7 \cdot H_2O$ nanobelts/reduced graphene oxide composites for aqueous zinc-ion batteries

Huili Cao,^{a*} Dr. Zhiyong Zheng,^a Prof. Poul Norby,^b Dr. Xinxin Xiao,^{a*} and Prof. Susanne Mossin^{a*}

^aDepartment of Chemistry, Technical University of Denmark, 2800 Kgs. Lyngby, Denmark

^bDepartment of Energy Conversion and Storage, Technical University of Denmark, 2800 Kgs. Lyngby, Denmark

Email: hucao@kemi.dtu.dk (Huili Cao); xixiao@kemi.dtu.dk (Xinxin Xiao);

slmo@kemi.dtu.dk (Susanne Mossin)

Keywords: Microwave-assisted; $V_3O_7 \cdot H_2O$ nanobelt; reduced graphene oxide; phase transition; zinc-ion battery.

$V_3O_7 \cdot H_2O$ nanobelts/reduced graphene oxide (rGO) composites (weight ratio: 86%/14%) are synthesized by a microwave approach with a high yield (85%) through controlling pH utilizing acids. The growth mechanisms of the highly crystalline nanobelts (average diameter: 25 nm; length: ca. 20 μm ; oriented along the [101] direction) have been thoroughly investigated, with the governing role of the acid upon the morphology and oxidation state of vanadium disclosed. When used as the ZIB cathode, the composite can deliver a high specific capacity of 410.7 and 385.7 mAh g^{-1} at the current density of 0.5 and 4 A g^{-1} , respectively, with a high retention of the capacity of 93%. The capacity of the composite is greater than those of $V_3O_7 \cdot H_2O$, V_2O_5 nanobelts, and $V_5O_{12} \cdot 6H_2O$ film. Zinc ion storage in $V_3O_7 \cdot H_2O$ /rGO is mainly a pseudocapacitive behavior rather than ion diffusion. The presence of rGO enables outstanding cycling stability up to 1000 cycles with a capacity retention of 99.6%. Extended cycling shows a gradual phase transition, *i.e.*, from the original orthorhombic $V_3O_7 \cdot H_2O$ to a stable hexagonal $Zn_3(VO_4)_2(H_2O)_{2.93}$ phase, which is a new electrochemical route found in V_3O_7 materials. This phase transition process provides new insight into the reactions of aqueous ZIBs.

1. Introduction

Lithium-ion batteries (LIBs) are commercially successful due to the high energy density and low self-discharge. However, lithium dendrite formation, high activity of the metallic lithium and the toxicity of the organic electrolytes cause safety and environmental concerns.[1] Alternatively, rechargeable multivalent ion batteries with earth-abundant elements (Mg, Al, Zn, etc.) are emerging. Among them, zinc-ion batteries (ZIBs) exhibit unique advantages: i) the aqueous electrolyte is either pH neutral or mildly acidic with a high ionic conductivity; ii) the zinc anode has a quite negative redox potential (-0.78 V vs. standard hydrogen electrode), leading to a high battery voltage (0.7-2.0 V)[2] and a considerable theoretical specific capacity of 820 mA g⁻¹. [3] However, hydrated Zn²⁺ cation has a large radius of 0.43 nm and exhibits sluggish transport kinetics in the active cathode materials, resulting in insufficient rate performance and low coulombic efficiency.[4] It is thus an urgent task to find a suitable cathode material with favourable capacity and stable structure during Zn²⁺ insertion and desorption. To date, the cathode materials of ZIBs can be divided into two categories: tunnel-type and layer-type structure.[5]

Multivalent manganese- and vanadium-based materials are promising cathode candidates.[6] A range of oxidation states of the metal are involved. The well-characterized MnO₂ undergoes stepwise reduction in battery reactions (*i.e.*, $2\text{Mn(IV)O}_2 + \text{Zn}^{2+} + 2\text{e}^- \rightleftharpoons \text{ZnMn(III)}_2\text{O}_4$; $\text{ZnMn(III)}_2\text{O}_4 + \text{Zn}^{2+} + 2\text{e}^- \rightleftharpoons 2\text{ZnMn(II)O}_2$).[7] The stepwise reduction is accompanied with phase transition. Tunnel-type MnO₂ (α -MnO₂, β -MnO₂, and γ -MnO₂) transforms into layered Zn-birnessite (Zn_xMnO₂) upon Zn²⁺ insertion. Layered-type δ -MnO₂ and spinel MnO₂ retain the same crystal structure during the insertion process. In comparison to MnO₂, vanadium-based materials have more oxidation states and crystal types, thus the insertion processes are even more complicated. Taking V₂O₅ as an example, the cathode reactions can be summarized as: $\text{V(V)}_2\text{O}_5 + \text{Zn}^{2+} + 2\text{e}^- \rightleftharpoons \text{ZnV(IV)}_2\text{O}_5$ or $\text{V(V)}_2\text{O}_5 + 2\text{Zn}^{2+} + 4\text{e}^- \rightleftharpoons \text{Zn}_2\text{V(III)}_2\text{O}_5$.[7]

corresponding to different theoretical capacities. To date, there are only a few reports disclosing phase transformation in V-based ZIB cathodes: Yang et al.[8] observed the formation of hexagonal $\text{Zn}_3(\text{OH})_2\text{V}_2\text{O}_7 \cdot 2\text{H}_2\text{O}$ among the orthorhombic V_2O_5 phase in the initial discharging cycle. The transformation was irreversible and barely contributed to the capacity in the following cycles. Recent reports only investigated the gradual phase change of V-based ZIB cathode for the initial several charge/discharge cycles,[9] using either *in situ* or *ex situ* characterizations. The gradual changes in the crystal phase during long-term cycles have not been investigated throughout, which are possibly responsible for the poor cycling performance of the cathode materials. It's proposed that i) the development of stable vanadium oxide based ZIB cathodes that can withstand long-term operation and ii) the detailed investigations of the phase transition during extended cycling which is one of key for making a significant progress for ZIB.

$\text{V}_3\text{O}_7 \cdot \text{H}_2\text{O}$ has a two-dimension crystal structure and a high capacity, and thus is a good candidate for the investigation. It is composed of layers of corner-sharing VO_6 octahedra and VO_5 square pyramids, where the layers interact through hydrogen bonding to the crystal water molecule, providing the position for the insertion and desertion of Zn^{2+} .[10] Furthermore, the presence of two oxidation states of vanadium ($\text{V}^{4+}/\text{V}^{5+}$) in $\text{V}_3\text{O}_7 \cdot \text{H}_2\text{O}$ improves the electronic conductivity compared to vanadium oxides with only one oxidation state,[11] due to the narrower bandgap (*e.g.* 2.0 eV for V_2O_5 ; 1.0 eV for V_3O_7). Most of the reported $\text{V}_3\text{O}_7 \cdot \text{H}_2\text{O}$ materials rely on a time-consuming hydrothermal process taking days,[12] posing the demand for more efficient fabrication methods.

A fast and energy-efficient synthesis allows the scale-up of production. Microwave-assisted heating is considered to be very efficient and energy-saving compared to traditional hydrothermal methods.[13] Herein, a high-yield one-step synthesis of $\text{V}_3\text{O}_7 \cdot \text{H}_2\text{O}$ and $\text{V}_3\text{O}_7 \cdot \text{H}_2\text{O}$ nanobelts/rGO composites by a microwave-assisted method is presented. *Ex situ* investigations

are applied to monitor the morphological evolution with time. $V_3O_7 \cdot H_2O$ nanobelts/rGO composite exhibited an ultra-long cycle life (99.6% capacity retention after 1000 cycles) in a potential range of 0.2-1.6 V vs. Zn^{2+}/Zn , making it possible to investigate the phase transition systematically. Cyclic voltammetry (CV), *ex situ* x-ray diffraction (XRD) and X-ray photoelectron spectroscopy (XPS) characterization have been applied towards this purpose.

2. Results and discussion

2.1. Characterizations of $V_3O_7 \cdot H_2O$ nanobelts and $V_3O_7 \cdot H_2O$ /rGO composites

The $V_3O_7 \cdot H_2O$ nanobelts and $V_3O_7 \cdot H_2O$ /rGO composites are synthesized through a microwave-assisted hydrothermal method by controlling pH with added acid (Figure S1). The reaction is maintained at 180 °C (Figure S1a). The morphology of the as-prepared products has been investigated by scanning electron microscope (SEM), atomic force microscope (AFM), and transmission electron microscope (TEM), see Figure 1. The as-prepared pure vanadium oxide exhibits a uniform nanobelt structure with a length of up to 20 μm in the SEM image (Figure 1a), and the mean width of the nanobelts is determined to be about 35 nm by TEM (Figure 1b). The strands are well-dispersed from each other. The typical thickness of the nanobelts is 20 nm measured by AFM (Figure 1c). The high resolution TEM (HR-TEM) image reveals the detail of the nanostructure. The nanobelts are highly crystalline, displaying lattice fringes with an interplanar spacing of ~ 0.36 nm corresponding to the (230) lattice planes of $V_3O_7 \cdot H_2O$ (Figure 1d) (ICOD: 00-028-1433).

During the fabrication process, graphene oxide (GO) is introduced to obtain a composite of vanadium oxide/reduced GO (rGO). The vanadium oxide is anchored on the surface of the rGO while retains the nanobelt morphology and the same dimensional features (Figure 1e). The HR-TEM image shows two interplanar spacings with an angle of $\sim 70^\circ$ with respect to each other (Figure 1f). The smaller interplanar spacing (0.36 nm) is indexed to be (230) and the other (0.85

nm) is (020), suggesting that the nanobelts are oriented along the [101] direction (*b*-axis oriented).

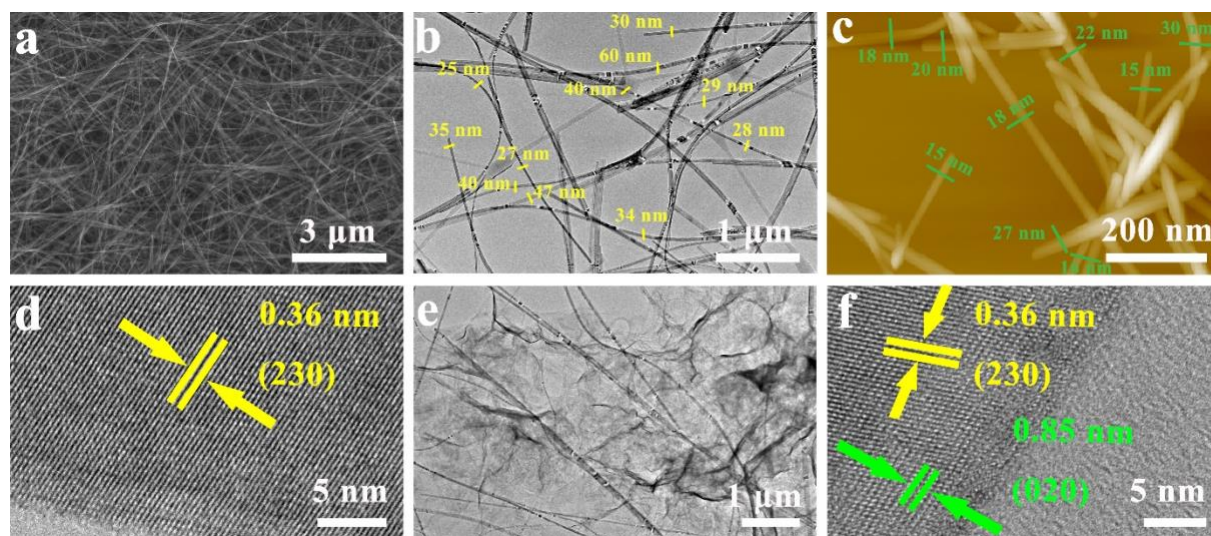


Figure 1 SEM (a), TEM (b), AFM (c), and HR-TEM images (d) of $V_3O_7 \cdot H_2O$ nanobelts. TEM (e) and HR-TEM (f) image of $V_3O_7 \cdot H_2O/rGO$ composite.

The typical XRD patterns of the $V_3O_7 \cdot H_2O$ nanobelts and $V_3O_7 \cdot H_2O/rGO$ have been characterized (Figure S2a). The pure nanobelts sample exhibits sharp peaks demonstrating high crystallinity, in consistency with the HR-TEM observation in Figure 1d. All peaks are in good agreement with the orthorhombic structure of $V_3O_7 \cdot H_2O$ (ICOD: 00-028-1433, $a = 9.34 \text{ \AA}$, $b = 17.00 \text{ \AA}$, $c = 3.62 \text{ \AA}$, $\alpha = \beta = \gamma = 90^\circ$). The peak at $2\theta = 24.7^\circ$ is assigned to (230) planes, as also observed in HR-TEM. $V_3O_7 \cdot H_2O/rGO$ presents all the characteristic peaks of the $V_3O_7 \cdot H_2O$ phase and an additional peak at $20\text{-}30^\circ$ corresponding to the (002) plane of disordered rGO nanosheets (Figure S3), [14] confirming again the successful preparation of the designed composite.

Thermogravimetric analysis (TGA) is performed to determine the weight ratio of rGO in the composites by increasing the temperature from 25 to 600 °C in a flow of air (Figure S2b and c). The TGA curve of $V_3O_7 \cdot H_2O$ shows a slight weight loss of ca. 2.5% at below 200 °C (Figure S2b), assigned to the release of adsorbed H_2O . [15] The weight loss of about 4.0% between 200 and 400 °C is due to the joint consequence of the crystal water loss in the $V_3O_7 \cdot H_2O$ precursor

and the weight gain due to the oxidation from V_3O_7 to V_2O_5 . $V_3O_7 \cdot H_2O/rGO$ exhibits a relative weight loss of 24% between 200 and 400 °C, with ca. 14% of the rGO decomposition, which is in consistency with the feed ratio for the synthesis.

As another important benchmark material, V_2O_5 is obtained by calcining $V_3O_7 \cdot H_2O$ nanobelts in air using a temperature ramp of 5 °C min^{-1} to 500 °C and maintaining 2 h at 500 °C. The nanobelts expand so that the diameter increases to 50-200 nm due to calcination-induced ripening, see Figure S4a. HR-TEM presents a typical lattice fringe spacing of around 0.58 nm, corresponding to the (020) crystal plane of V_2O_5 (Figure S4b). XRD further confirms the phase purity of orthorhombic V_2O_5 (Figure S4c) (COD: 01-085-0601).

2.2. Mechanism of the $V_3O_7 \cdot H_2O$ nanobelt formation

The $V_3O_7 \cdot H_2O$ nanobelts are produced via a facile one-step microwave treatment of $VOSO_4 \cdot xH_2O$ at acidic conditions. To investigate the governing factors for the formation of nanobelt morphology, control experiments have been carried out by varying the time and the identity of the acid used for the synthesis. First, the evolution in morphology with time is examined. As shown in Figure 2a, the product obtained after 10 min microwave reaction shows a cubic structure consisting of sheets with an average size of 1 μm . The HR-TEM image shows sheets of uniform thickness with edges gradually rolling into nanobelts with poor crystallinity (Figure S5). The interplanar spacing of sheets is determined to be 0.36 nm corresponding to the (230) planes of the $V_3O_7 \cdot H_2O$ (Figure S5a). After 60 min of reaction (Figure 2b), the cubic structure is stretched into sheets and the nanobelts become more obvious. HR-TEM further confirms that the $V_3O_7 \cdot H_2O$ nanobelts grow along the *b*-axis. Extending the reaction time to 80 min, more nanobelts are formed and the boundaries of the sheet are shrinking into a needle-like morphology (Figure 2c). The final products, *i.e.*, $V_3O_7 \cdot H_2O$ nanobelts with a length of 20 μm , are obtained after 120 min of reaction (Figure 1b).

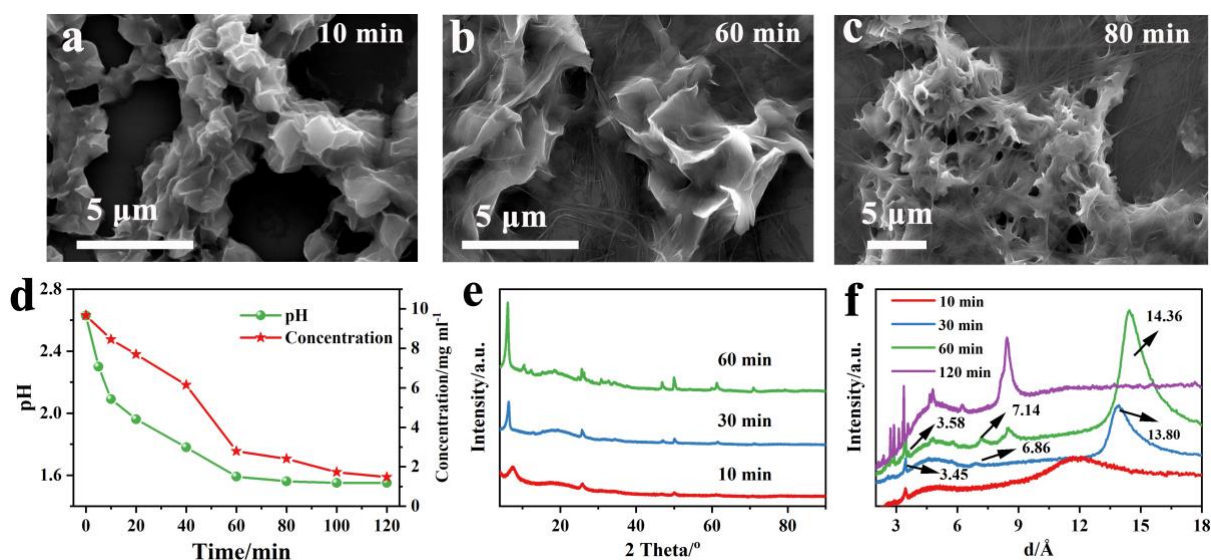
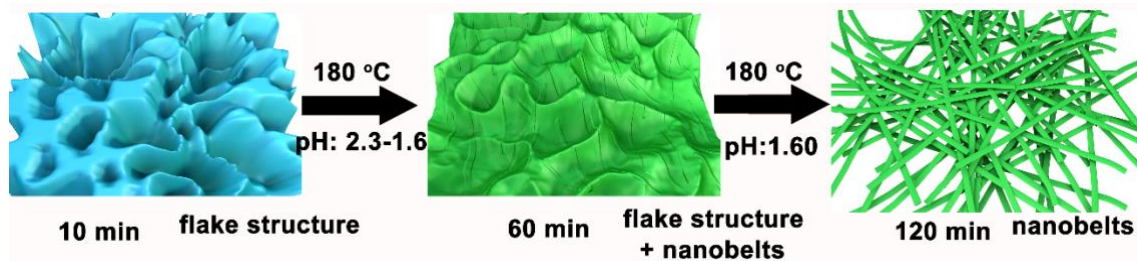


Figure 2. SEM images of $V_3O_7 \cdot H_2O$ obtained at 10 (a), 60 (b) and 80 min (c); time profiles (d) of the corresponding $VOSO_4$ concentration and pH; XRD patterns (e) of the product at 30 and 60 min and (f) converted XRD patterns obtained from Fullprof software.

Using *ex-situ* UV-Vis spectroscopy of the supernatant, it is straightforward to monitor the reaction due to the prominent d-d transitions of oxidovanadium(IV), VO^{2+} in the 760-780 nm range (Figure S6).[16] The absorbance of VO^{2+} decreases as the reaction proceeded (Figure S6a). The initial 40 min shows a consumption rate of VO^{2+} of about 0.08 mg min^{-1} , as referred to the standard calibration curve in Figure S6c. The reaction rate is doubled in the following 20 min, whereas the final 60 min shows a rather slow reaction with $[VO^{2+}]$ concentration being almost constant. The pH decreases steadily and stabilized at 1.60 in the final stage (Figure 2d). Up to 85% of the initially fed vanadium is converted into the final product, implying that the microwave-assisted synthesis is a high yield method.

XRD is applied to investigate the phase transition (Figure 2e). The crystallinity increases with the reaction time. Most of the prominent peaks can be assigned to $V_3O_7 \cdot H_2O$ (ICOD: 00-028-1433). To precisely identify the $V_3O_7 \cdot H_2O$ phase, converted XRD patterns associated with lattice space are obtained using Fullprof software (Figure 2f).[17] The analysis shows that the peaks at 3.45, 6.86 and 13.80 nm in the sample obtained at 30 min are due to the layer structure. After 60 min of reaction, the $V_3O_7 \cdot H_2O$ phase is dominant and the interlayer spacing increased to 3.58, 7.14 and 14.36 nm. After 2 h of reaction, the peaks due to the layer structure disappeared.

Scheme 1 illustrates the suggested nanobelt formation mechanism, where 2D sheets are obtained in the beginning, forming nanobelts while growing. As the reaction proceeds, the vanadium in solution is nearly depleted, and pH drops and stabilizes at about 1.60. The suggested formation process of the $V_3O_7 \cdot H_2O$ nanobelt morphology is illustrated in Scheme 1.



Scheme 1 Diagram illustrating the formation process of $V_3O_7 \cdot H_2O$ nanobelts.

Based on the above *ex situ* investigation, the mechanism of $V_3O_7 \cdot H_2O$ nanobelt formation *via* microwave treatment can be summarized as:



VO^{2+} is oxidized by O_2 in the atmosphere at high temperature, which produces H^+ and thus reduces pH. The presence of O_2 during the hydrothermal reaction is often necessary to obtain metal oxides with high oxidation states.[18] This assumption is validated by the control experiment showing that the reaction is hindered without O_2 (Figure S7). It is also hindered when the initial pH is lower than 1.8, regardless of the atmosphere (Figure S8).

The identity of the acid is also a key factor. Control experiments (Figure S9) with the addition of HCl, CH_3COOH (HAc) and H_2SO_4 resulted in dark cyan suspensions, while the addition of HNO_3 leads to a dark brown suspension. The sample fabricated without the addition of any acids (initial pH = 3.0) presents nanobelt morphology, but with a wide range of diameter distribution and large particles with a size of 10 μm . When the pH is controlled by HAc and HCl, more uniform and longer nanobelts are obtained (Figure S10b and c). In comparison, the use of HNO_3 results in a pure film structure (Figure S10d).

XPS analysis of different acid-derived samples is applied for a detailed understand the effect of acid on the chemical composition and oxidation state of vanadium. The survey spectra of all

the samples found three main elements (V, O, and C) present (Figure 3a). The high-resolution spectra of V2p and O1s show that the samples obtained with HAc, H₂SO₄, HCl have similar V2p peaks (Figure 3b). Taking H₂SO₄ as a representative, the peaks at 517.2 and 525.0 eV are assigned to V2p_{2/3} and V2p_{1/3} from V⁵⁺, with a peak separation of about 7.8 eV.[19] The peaks at 515.7 and 523.5 eV are assigned to V⁴⁺ (Figure 3c).[20] In contrast, the HNO₃ derived sample and V₂O₅ (Figure 3b) both display strong peaks at 517.2 and 525.0 eV assigned to V⁵⁺ and only very weak peaks assigned to V⁴⁺, suggesting the majority of the vanadium are in the oxidation state +5.[21]

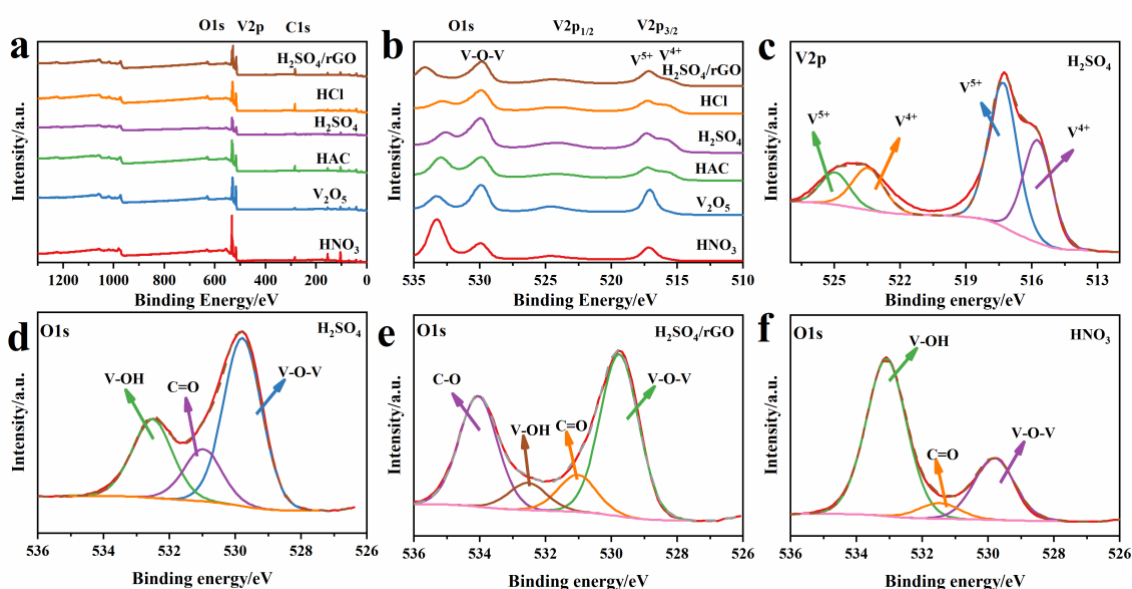


Figure 3. XPS survey spectra (a), O1s, and V2p spectra (b) of all samples; high-resolution V2p spectrum (c) and (d) O1s spectrum of the H₂SO₄ derived sample. O1s spectrum of the V₃O₇·H₂O/rGO composite (e) and the HNO₃ derived sample (f).

Based on the O1s spectra, the samples can be divided into three categories. The samples obtained with strong acids, HCl, and H₂SO₄, presents peaks at 529.8, 531.0 and 532.5 eV after deconvolution corresponding to V-O-V, C=O and V-OH, respectively.[22] The C=O peak might originate from CO₂, and V-OH is from the crystal water in the product and from moisture. For the V₃O₇·H₂O/rGO composite (Figure 3e), there is an additional peak at 534.0 eV,[23] which is assigned to C-O. The weak acid HAc leads to the sample with a stronger O1s peak from V-OH compared to the strong acid-derived samples (Figure 3b and f). For the samples derived from V₂O₅ or HNO₃, the V-OH peak shifts to a higher binding energy, *i.e.*, from 532.5

to 533.1 eV. This observation might be related to the crystal water, especially in the film structure present in the HNO₃ derived sample. The presence of a strong hydroxyl signal in the product is also reported in other film structure materials.[24]

X-ray diffraction is applied to identify the crystal structure and phase purity of the as-prepared samples. All peaks of the samples derived from H₂SO₄, HAc, or HCl are indexed to be V₃O₇·H₂O (ICOD: 00-028-1433) (Figure S11a). In contrast, the diffraction patterns of the HNO₃ derived product are indexed to be the monoclinic phase of V₅O₁₂·6H₂O (JCPDS 45-1401) with C2/m(12) space group (Figure S11b). The strongest peak is at 2θ = 7.5°, corresponding to the (001) plane. V₅O₁₂·6H₂O has 4 out of 5 vanadium in oxidation state +5, suggesting that the oxidizing property of HNO₃ affects the vanadium oxidation states and thus the phase formation.

2.3. Electrochemical performance of V₃O₇·H₂O/rGO and V₃O₇·H₂O nanobelt

The electrochemical properties of the as-prepared V₃O₇·H₂O and V₃O₇·H₂O/rGO nanobelts are investigated by cyclic voltammetry (CV) at a scan rate of 0.1 mV s⁻¹ in a voltage window of 0.2-1.6 V. The first cycle of V₃O₇·H₂O shows much broad peaks, which gradually disappears in the following cycle. It might be due to either an initial activation process of the fresh electrolyte or a phase transition similar to that found in LIBs (Figure 4a and S12).[25] To explore the reactions in pure V₃O₇·H₂O, a narrow potential range of 0.4-1.1 V is used for following test, see Figure S12c. There are two main pairs of redox peaks (0.76 /0.87 V and 0.51 /0.61 V) for V₃O₇·H₂O, demonstrating a multi-step insertion/desertion mechanism.[26] The curves also confirms that the voltage window of 0.4-1.1 V (vs. Zn/Zn²⁺) for V₃O₇·H₂O nanobelts is suitable. In sharp comparison, the initial cycle of V₃O₇·H₂O/rGO, however, well overlaps with the subsequent cycles. Additional peaks can be observed at 0.96/1.04 V, 0.88/0.98 V, 0.72/0.81 V and 0.35 /0.58 V in V₃O₇·H₂O/rGO. These peaks are well known in pure V₂O₅ and VO₂ structures.[8, 27] In comparison to V₃O₇·H₂O, V₃O₇·H₂O/rGO composites exhibit more peaks,

which are indicative of the importance of rGO for attracting more Zn^{2+} ions to (de)insertion in the host structure.

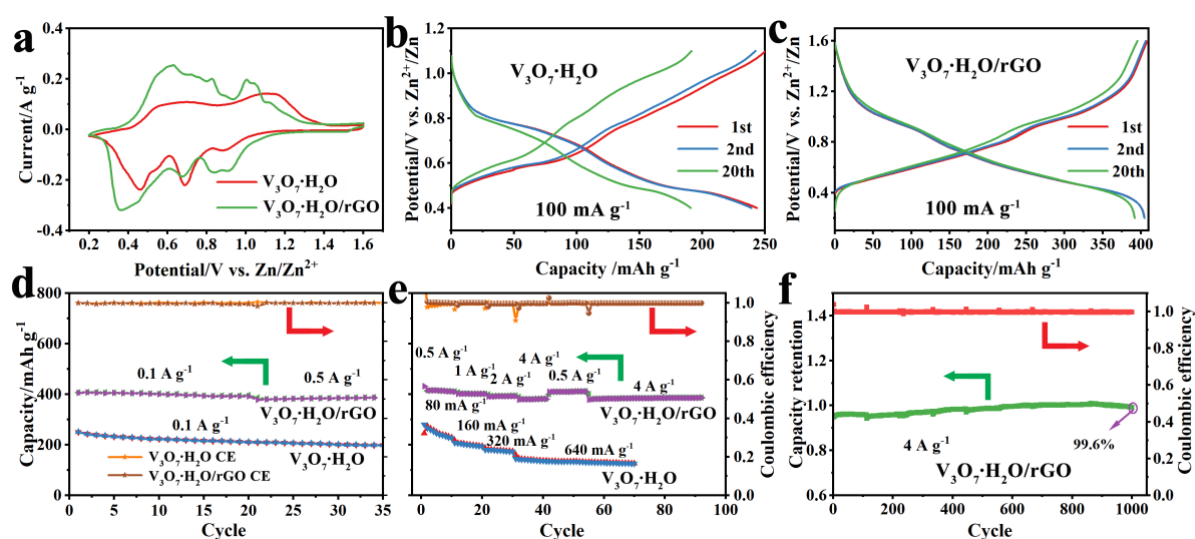


Figure 4. Initial CV curves (a) of $\text{V}_3\text{O}_7\cdot\text{H}_2\text{O}$ and $\text{V}_3\text{O}_7\cdot\text{H}_2\text{O}/\text{rGO}$ at a scan rate of 0.1 mV s^{-1} ; galvanostatic charge/discharge profiles of $\text{V}_3\text{O}_7\cdot\text{H}_2\text{O}$ (b), and $\text{V}_3\text{O}_7\cdot\text{H}_2\text{O}/\text{rGO}$ (c) at a current density of 100 mA g^{-1} ; cycling performance (d) and rate capability (e) of the $\text{V}_3\text{O}_7\cdot\text{H}_2\text{O}$ and $\text{V}_3\text{O}_7\cdot\text{H}_2\text{O}/\text{rGO}$; long-term cycling performance (f) of the $\text{V}_3\text{O}_7\cdot\text{H}_2\text{O}/\text{rGO}$ at a current density of 4 A g^{-1} .

To investigate the electrochemical stability and capacity retention, the performance and coulombic efficiency of $\text{V}_3\text{O}_7\cdot\text{H}_2\text{O}$ and $\text{V}_3\text{O}_7\cdot\text{H}_2\text{O}/\text{rGO}$ are tested during extended cycling.

$\text{V}_3\text{O}_7\cdot\text{H}_2\text{O}$ shows an initial discharge capacity of 243.6 mAh g^{-1} with a coulombic efficiency of 97.2%. Two obvious repeatable voltage plateaus are found in the potential range of 0.9-0.7 V and 0.4-0.6 V, corresponding to the redox peaks of the CV curves (Figure 4a). The specific capacity of $\text{V}_3\text{O}_7\cdot\text{H}_2\text{O}$ decreases to 210.9 mAh g^{-1} after 20 cycles at 100 mA g^{-1} (86.6% retention), which further gradually decreases to 198.8 mAh g^{-1} at 35 cycles (Figure 4d). The degradation of capacity is likely due to the structure change upon Zn^{2+} insertion and consequent lattice distortion and loss of active sites.[28] In comparison, $\text{V}_3\text{O}_7\cdot\text{H}_2\text{O}/\text{rGO}$ exhibits a much higher initial capacity of 404.7 mAh g^{-1} with a coulombic efficiency of 99.0% (Figure 4c). In the subsequent cycles, the charge-discharge profiles are almost identical, with a specific capacity of 391.9 mAh g^{-1} (96.8% retention) after 20 cycles. At a high current density of 500 mA g^{-1} (Figure 4d), $\text{V}_3\text{O}_7\cdot\text{H}_2\text{O}/\text{rGO}$ still delivers a high specific capacity of 386 mAh g^{-1} with

a retention ratio of 95.3% of the initial capacity, indicating excellent structural stability of the composite material. Additionally, the coulombic efficiency of both $V_3O_7 \cdot H_2O$ and $V_3O_7 \cdot H_2O/rGO$ are stabilized at approximately 100% during the cycling testing, suggesting a highly reversible reaction process. When applied $V_3O_7 \cdot H_2O$ cathode in the wide potential range of 0.2-1.6 V, the voltage plateaus disappear, and it only delivers ca. 100 mAh g^{-1} , compared to over 400 mAh g^{-1} with clear plateaus of $V_3O_7 \cdot H_2O/rGO$ (Figure S12d and e). After 20 cycles, the capacity decreases to a level of lower than 100 mAh g^{-1} .

The rate performance is given in Figure 4e. The discharge capacities of $V_3O_7 \cdot H_2O$ nanobelts are 227.3, 194.1, 173.9, and 126.1 mAh g^{-1} at current densities of 80, 160, 320, and 640 mA g^{-1} , respectively. The specific capacity shows a downward trend, and the capacity at 640 mA g^{-1} is only about 55% of that at 80 mA g^{-1} . Distinguishably, $V_3O_7 \cdot H_2O/rGO$ exhibits reversible capacities of 410.7, 401.1, 391.7, and 380.4 mAh g^{-1} at much higher current densities of 0.5, 1, 2, and 4 A g^{-1} , respectively. Impressively, the capacity is 411.5 mAh g^{-1} when the current density is returned to 0.5 A g^{-1} . Even upon a current density of 4 A g^{-1} , a considerable capacity of 385.7 mAh g^{-1} is registered. The retained capacity ratio is 94% when increasing the current density from 0.5 to 4 A g^{-1} . It is concluded that $V_3O_7 \cdot H_2O/rGO$ composites exhibit a highly stable structure during the significant current fluctuation, leading to a very stable performance during long-term cycling (Figure 4f). The $V_3O_7 \cdot H_2O/rGO$ composite shows a retained capacity of 99.6% and a coulombic efficiency at nearly 100% upon 1000 cycles at 4 A g^{-1} .

The electron transfer resistance of the active material interfaces is investigated by electrochemical impedance spectroscopy (EIS) at the open-circuit voltage before and after cycling testing (Figure S13). The Nyquist plots display two small semicircles in the high-frequency region and a straight line in the low-frequency region. The diameter of the semicircle reveals the charge-transfer impedance (R_{ct}) from anode and cathode, while the straight line at the low-frequency region is related to the Zn^{2+} diffusion process in the electrolyte. Before

cycling, the Rct of V₃O₇·H₂O is about 529 Ω, twice that of V₃O₇·H₂O/rGO. After cycling, V₃O₇·H₂O/rGO shows Rct = 21.6 Ω, which is only ~10 % of that of V₃O₇·H₂O (206.3 Ω). The linear fitting of the Warburg impedance with the real part Z' shows that V₃O₇·H₂O/rGO has a small slope of the line before and after cycling, suggesting a low Warburg coefficient and a fast metal ion diffusion coefficient. Based on the Warburg coefficient, the zinc ion diffusion coefficient in the interfacial region, D, can be calculated using the following equations:[29]

$$D = \frac{R^2 T^2}{2(A n^2 F^2 C_{Zn} \sigma)^2} \quad (2)$$

$$Z_{re} = R_{ct} + R_s + \sigma \omega^{-0.5} \quad (3)$$

where R is the gas constant (8.314 J mol K⁻¹), T the temperature (298 K), A the surface area of the electrode (1.77 cm²), F the Faraday constant (96500 C mol⁻¹), C_{Zn} the concentration of zinc ion (0.003 mol cm⁻³), and σ the Warburg factor obtained from Figure S13b. Thus, the zinc ion diffusion coefficient for V₃O₇·H₂O/rGO composite after cycling is calculated to be ca. 6.5×10⁻¹¹ cm² s⁻¹, about 100 times higher than that of pure V₃O₇·H₂O. It suggests that rGO can effectively enhance the kinetics of the electron transfer in electrodes and facilitate electrolytic infiltration and diffusion of Zn²⁺.

For comparison, the other as-prepared vanadium oxides (V₂O₅ nanobelts and V₅O₁₂·6H₂O film), as well as pure rGO, are investigated as ZIB cathodes (Figure S14). CV curves of V₂O₅ show multiple redox peaks, which become intensified after the initial cycle due to the trapped Zn²⁺ ions acting as interlayer pillars.[30] This matches well with the galvanostatic charge/discharge curves with increased capacity upon cycling. Specifically, the discharge capacity of the V₂O₅ nanobelts climbs from 36 to 286 mAh g⁻¹ after 30 cycles at 100 mA g⁻¹, implying that an activation process occurred during the first several cycles.[31] The rate performance is poor with only 31% capacity retention when amplifying the current density from 100 to 800 mA g⁻¹. The coulombic efficiency is approximately 86% at 800 mA g⁻¹. The discharge voltage plateaus of the V₅O₁₂·6H₂O film during the charge and discharge process are ca. 0.95 V and 0.42 V, corresponding well with the redox peaks in the CV curve (Figure S15a and b). Even

after 20 cycles, the voltage plateaus are still obvious, revealing a high reversibility during the reaction process.[32] In the 50th cycle, the specific capacity at a current density of 100 mA g⁻¹ is 46.3 mAh g⁻¹. The pure rGO material is obtained by the same microwave method, but without introducing VOSO₄. There is no obvious voltage plateau in the charge-discharge curves, neither peak, in the CV curve (Figure S15d and e), suggesting that the dominant contribution to the capacity is from the electrochemical double layer. The specific capacity of pure rGO reaches 62.8 mAh g⁻¹ (Figure S15f), 6.5 times lower than that of V₃O₇·H₂O/rGO. These control experiments indicate that the mixed oxidation state of vanadium can help to overcome the sluggish Zn²⁺ diffusion kinetics and lead to a high coulombic efficiency. The electrochemical behaviors of the cathode are also possibly affected by the morphology and the amount of crystal water.[33]

V₃O₇·H₂O/rGO also outperforms most reported vanadium oxide materials, see Table S1. Benchmark materials such as hollandite-type Al-doped VO_{1.52}(OH)_{0.77} obtained by solvothermal synthesis delivered 105 mAh g⁻¹ at a current density of 0.015 A g⁻¹. [34] Freestanding graphene/VO₂ composites, fabricated *via* freeze-drying, high-temperature reduction and subsequent mechanical compression, had a reversible capacity of 240 mAh g⁻¹ at a current density of 4 A g⁻¹. [27] Ultrafine nanogrid-shaped layered V₃O₇·H₂O arched on carbon synthesized by *in situ* electrochemical oxidation delivered 481.3 mAh g⁻¹ at a current density of 0.1 A g⁻¹. The reversible capacity, however, decreased to 171.6 mAh g⁻¹ at a high current density of 5 A g⁻¹. [35] In brief, the V₃O₇·H₂O nanobelt/rGO composites are a promising high-performance ZIB cathode candidate, featuring fast electron transfer in the materials at high current densities.

2.4. Investigation of the reaction mechanism of V₃O₇·H₂O/rGO cathode

The multiple redox reactions of vanadium with more feasible Zn²⁺ ion insertion is believed to be the reason for the considerable specific capacity. To distinguish the capacity current

distribution from either diffusion or faradaic contribution, CV is conducted at various scan rates from 0.1 to 0.8 mV s⁻¹ (Figure 5a). It is noted that with increasing scan rate, the CV curves feature broader peaks but still maintain the similar shape. The relationship between the peak current (*i*) and the scan rate (*v*) can be described by the following equation:

$$i = av^b \quad (4)$$

where ‘b’ is a parameter between 0.5 and 1. When the results are fitted using this equation and the resulting fitted ‘b’ parameter is close to 0.5, it is an indication that the process is dominated by ion diffusion; when ‘b’ approaches 1, the reaction is best characterized as a faradaic process.[36] Based on the fitting of log *i* vs log *v*, the values of ‘b’ for the four main peaks can be calculated to be 0.99, 0.94, 0.88 and 0.86, respectively (Figure 5b). In addition, the reversible capacity contribution of the V₃O₇·H₂O/rGO composite is further quantitatively evaluated according to the following equation:[37]

$$i = k_1v + k_2v^{1/2} \quad (5)$$

where ‘k₁’ and ‘k₂’ are constants, associated with the intercalation capacity contribution and diffusion contribution, respectively. The intercalation capacity contribution gradually increases from 90% to 99% with scan rate in a range of 0.1-0.8 mV s⁻¹ (Figure S16), suggesting the dominant faradaic effect. The intercalation capacitive contribution of V₃O₇·H₂O/rGO composite is much higher in comparison to other reported layered V-based cathodes, such as V₂O₅/polyaniline,[38] Mn_{0.15}V₂O₅·nH₂O,[39] (NH₄)₂V₄O₉,[40] which might be due to the low electron transfer resistant and the fast diffusion coefficient in the electrode.

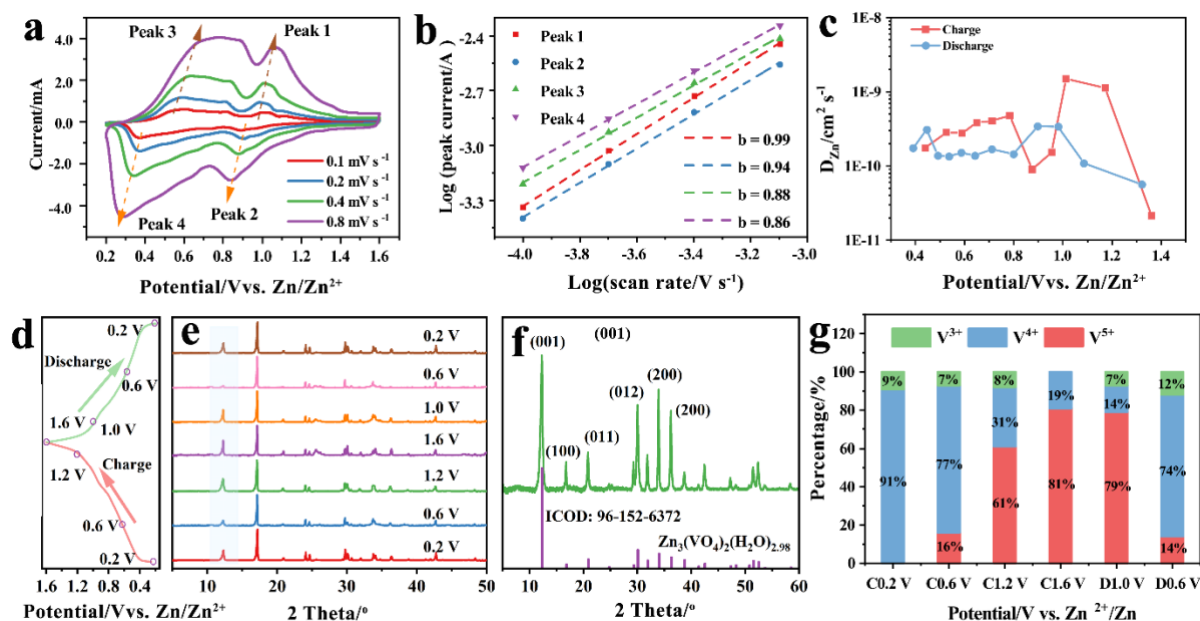


Figure 5 CVs of $V_3O_7 \cdot H_2O/rGO$ at different scan rates from 0.1 to 0.8 $mV s^{-1}$ (a); $\log i$ vs. $\log v$ plots of the oxidation and reduction peaks of the electrode (b); Zn^{2+} coefficient of the $V_3O_7 \cdot H_2O/rGO$ cathode as a function of working potential during CD testing (c). ex situ XRD patterns of $V_3O_7 \cdot H_2O/rGO$ at different charge/discharge states of the 11th cycle (d, e); XRD patterns of $V_3O_7 \cdot H_2O/rGO$ after 1000 cycles (f). Oxidation state of vanadium in $V_3O_7 \cdot H_2O/rGO$ during the charge (C) and discharge process (D) at different voltages calculated from the V2p peak of the XPS spectra (g).

Very interestingly, it is found that the 11th CV curve shape obtained at 0.8 $mV s^{-1}$ differs from the previous cycles, seeing that the major cathodic peak shifts from 0.57 to 0.67 V and the minor peak at ca. 1.1 V disappear (Figure S17). The same changes are also visible at 0.1 $mV s^{-1}$. In addition, the shape of the forward scan (1.6 to 0.2 V) in the first cycle differed from the following scans and also from the one found in the literature for $V_3O_7 \cdot H_2O/rGO$. It can be concluded that, unlike the reported insertion mechanism for vanadium oxides,[41] a phase transition during operation is the most likely explanation for the observed CV characteristics of the $V_3O_7 \cdot H_2O/rGO$ electrode.

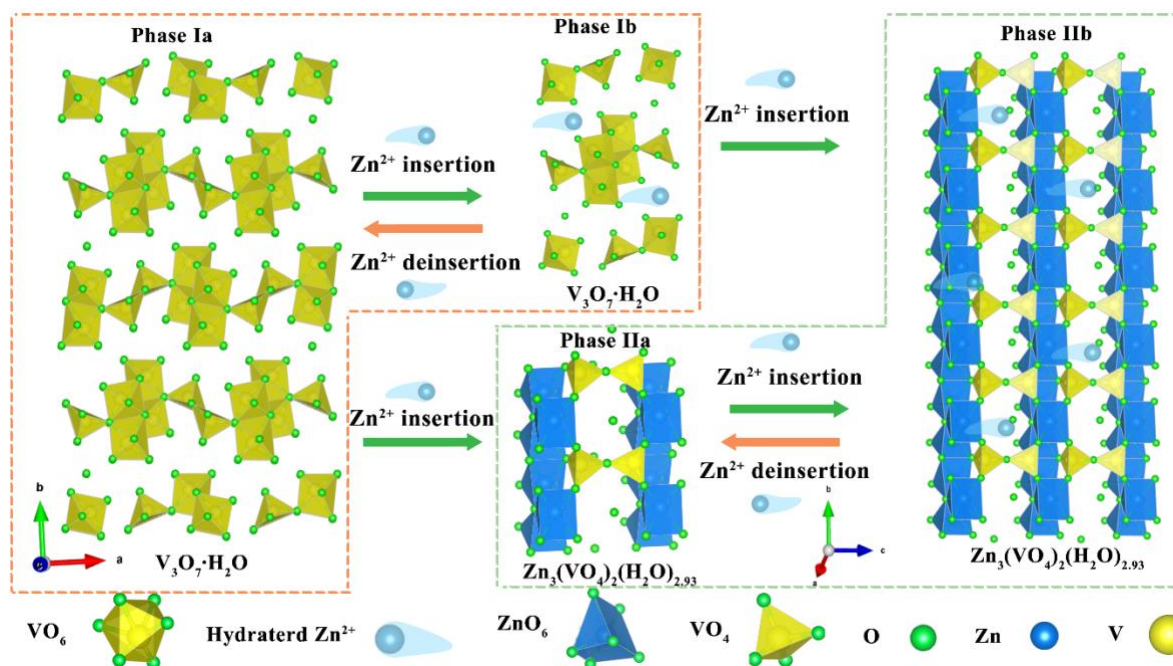
Ex situ XRD and XPS are employed to investigate this hypothesis further in Figure S18 and 19. For this investigation, a thin layer of 0.5 $mg cm^{-2}$ of the active materials has been applied on the electrode to guarantee a full utilization. In comparison, 1.3 $mg cm^{-2}$ is used for routine investigations. XRD patterns of $V_3O_7 \cdot H_2O/rGO$ are obtained at different discharge stages (1.0, 0.6 and 0.4 V) of the initial cathodic scan at 0.1 $mV s^{-1}$. Overall, the XRD peaks of $V_3O_7 \cdot H_2O$

transform from being sharp to broad, due to the collapse of the original structure and the formation of a new phase. Upon initial discharge to 1.0 V, the main peak at 10.4°, belonging to (020), disappears. Further discharging to 0.4 V, it results in the appearance of new peaks at 12.3°, 30.1°, and 36.5° corresponding to (001), (012), and (021) of hexagonal $\text{Zn}_3(\text{VO}_4)_2(\text{H}_2\text{O})_{2.93}$ ($a = b = 6.05 \text{ \AA}$, $c = 7.195 \text{ \AA}$, $\alpha = \beta = 90^\circ$, $\gamma = 120^\circ$, ICOD:96-152-6372). Those results confirm the phase transition during Zn^{2+} discharge/insertion. The associated XPS V2p spectrum shows that at 1.0 V, +5 is the dominant oxidation state of vanadium, see Figure S18a. Upon further discharged to lower potentials (0.6 and 0.4 V), the amount of V^{4+} and V^{3+} increases (Figure S19b and c), verifying the change in vanadium oxidation state in $\text{V}_3\text{O}_7\cdot\text{H}_2\text{O}/\text{rGO}$ alongside the phase transition. The quantitative peak-fitting analysis of the V2p spectra from XPS show that the dominant V^{5+} decreases from 53% to 5% under a backward scan (from 1.0 to 0.4 V), corresponding to the insertion of about 0.5 mol Zn^{2+} into 1 mol $\text{V}_3\text{O}_7\cdot\text{H}_2\text{O}$. The galvanostatic intermittent titration technique (GITT, the detailed measurements are shown in SI, Figure S21) is also employed to calculate the Zn^{2+} ion diffusion coefficient in $\text{V}_3\text{O}_7\cdot\text{H}_2\text{O}/\text{rGO}$ composite (Figure 5c). It is noted that the diffusion coefficient of Zn^{2+} ion in the active material during the entire insertion and desertion process is in the range of 10^{-10} - $10^{-9} \text{ cm}^2 \text{ s}^{-1}$, which is higher than the Zn^{2+} diffusion in other vanadium-based cathode materials.[42] To understand the different CV features of the 11th charge/discharge cycle, *ex situ* XRD and XPS are applied. To obtain better XRD signals, an increased mass loading of the active materials (1.3 mg cm^{-2}) is employed at a current density of 50 mA g^{-1} . The 11th charge/discharge cycle is not connected, and an obvious shift of the XRD peaks at different charge/discharge status is observed, whereas the peak intensity at 12.3° corresponding to the (001) plane becomes stronger under the charging process. The latter is associated with insertion of Zn^{2+} (Figure 5e). The evolution in the oxidation state of vanadium during the charge and discharge process is also studied *by ex situ* XPS (Figure S20). In the Zn 2p region, the Zn 2p_{1/2} and Zn 2p_{3/2} peaks

in the discharge state (0.2 V) are obvious, due to Zn^{2+} insertion. Upon charging, however, these two peaks are still present but with lower intensity, suggesting that residual zinc ions are present even after Zn^{2+} extraction. The V2p spectra at the fully discharged state (0.2 V) display a strong V^{4+} peak and a weak V^{3+} peak, suggesting a significant reduction of V_3O_7 . Upon recharge, the V^{5+} peaks appear and become gradually stronger, corresponding to the extraction of Zn^{2+} . The discharge process, on the other hand, shows the opposite trend, indicating that Zn^{2+} insertion and desorption in V_3O_7 are close to being reversible. The amount of vanadium in different oxidation states during the charge and discharge process is quantified by analyzing the V2p spectra (Figure 5g). By calculating the amount of Zn^{2+} ions inserted, there is about 1.4 mmol Zn^{2+} for each mol of $\text{V}_3\text{O}_7 \cdot \text{H}_2\text{O}$ participating in the redox reactions. This corresponds to a high specific capacity of 265 mAh g^{-1} by only considering the contribution from the faradic capacity. It further confirms that the $\text{V}_3\text{O}_7 \cdot \text{H}_2\text{O}/\text{rGO}$ for Zn^{2+} storage process is dominated by pseudocapacitive behavior rather than ion diffusion and the new phase of $\text{Zn}_3(\text{VO}_4)_2(\text{H}_2\text{O})_{2.93}$. It is likely due to the activation of the active materials and the reversible phase transition. The composition of crystalline phases in $\text{V}_3\text{O}_7 \cdot \text{H}_2\text{O}/\text{rGO}$ is investigated after 1000 cycles. The initial orthorhombic $\text{V}_3\text{O}_7 \cdot \text{H}_2\text{O}$ phase is transformed completely to a phase-pure hexagonal $\text{Zn}_3(\text{VO}_4)_2(\text{H}_2\text{O})_{2.93}$ (Figure 5f). This development is attributed to the presence of rGO, which enables a highly stable cycling performance.

Both of $\text{V}_3\text{O}_7 \cdot \text{H}_2\text{O}$ (phase I) before phase transition and $\text{Zn}_3(\text{VO}_4)_2(\text{H}_2\text{O})_{2.93}$ (phase II) after phase transition undergo the Zn^{2+} insertion mechanism without changing the crystal structure. A hypothesis for the Zn^{2+} insertion and desorption process in the host vanadium oxide cathode, which is in agreement with all results, are summarized in Scheme 2. In the initial discharge process, hydrated Zn^{2+} ions intercalate into the $\text{V}_3\text{O}_7 \cdot \text{H}_2\text{O}$ (phase Ia) structure layers forming phase Ib, and further discharge leads to a partial phase transition to $\text{Zn}_3(\text{VO}_4)_2(\text{H}_2\text{O})_{2.93}$ (phase IIa and b). During the initial charge process, reversible Zn^{2+} desorption takes place converting

the phase Ib to phase Ia, and phase IIb is transformed back into the phase IIa. With extended cycling, more of the phase II forms, until the cycles are ultimately dominated by the reversible transition between the phase IIa and phase IIb. Such a new discovery of phase transition is unique, which promotes the understanding of underlying mechanism of layered $V_3O_7 \cdot H_2O$ for long-term and stable cycling.



Scheme 2 Illustration of the phase transition during Zn^{2+} ion insertion and desorption. The conversion in the pink and green dash box governs the initial cycles and long-term cycling, respectively.

3. Conclusion

In summary, the combination of $V_3O_7 \cdot H_2O$ and rGO has been achieved by a facile microwave-assisted approach. For the preparation of $V_3O_7 \cdot H_2O$ nanobelts material, it is found that two-dimensional layered flakes form initially, which stretch into films and finally into nanobelts. This process is independent of the choice of acid for pH control as long as the acid is not oxidizing. When applied as the cathode electrode of zinc-ion batteries, the $V_3O_7 \cdot H_2O/rGO$ composite exhibits a much better retention of capacity and rate performance, compared to pure $V_3O_7 \cdot H_2O$ nanobelts, V_2O_5 nanobelts, and $V_5O_{12} \cdot 6H_2O$ films. This is mainly due to the presence of rGO, which improves the electron transfer kinetics. The combination with rGO makes it

possible to extend the cycling performance of $V_3O_7 \cdot H_2O$ up to 1000 cycles, leading to the identification of the gradual phase transition: from orthorhombic $V_3O_7 \cdot H_2O$ to hexagonal $Zn_3(VO_4)_2(H_2O)_{2.93}$. The final reversible phase transition between an intermediate phase and hexagonal $Zn_3(VO_4)_2(H_2O)_{2.93}$ paves the way for screening highly stable zinc vanadate ($Zn_3(VO_4)_2$).

4. Experimental Section

Chemicals: Potassium persulfate ($K_2S_2O_8$, 99%) was bought from Ferak. Graphite, phosphorous pentoxide (P_2O_5 , 98%), sulfuric acid (H_2SO_4 , 95%-97%), concentrated hydrochloric acid (HCl, 37% w/w, diluted to 1.0 M), 1-methyl-2-pyrrolidinone (C_5H_8NO , NMP, 99.5%), poly(vinylidene fluoride) (PVDF, $(CH_2CF_2)_n$, average MW ~534,000), vanadium oxide sulfate hydrate ($VO_4 \cdot xH_2O$, 97%), nitric acid, zinc trifluoromethanesulfonate ($Zn(CF_3SO_3)_2$, 98%), and zinc foil (thickness: 0.25 mm, 99.9%) were purchased from Sigma-Aldrich, Denmark. Potassium permanganate ($KMnO_4$, 99.9%) and hydrogen peroxide (H_2O_2 , 30 wt%) were bought from Merck. Potassium hydrogenphosphate (K_2HPO_4 , 99.99%) and carbon black (99.9%) were from Fluka. Steel meshes were obtained from Lizhiyuan Co., Ltd, China.

Synthesis of $V_3O_7 \cdot H_2O$ nanobelts/reduced GO: 0.5 mmol $VO_4 \cdot xH_2O$ was dissolved into 10 mL Milli-Q to form a clear blue solution, into which 0.1 M H_2SO_4 was added to adjust the pH to 2.6-2.7. After stirring for 2 h, 1 mL as-prepared GO solution (see supporting information) was added into the solution, which was sealed in a 35 mL microwave tube and heated up to 180 °C for 2 h in a Biotage® microwave reactor. The reaction parameters were monitored during the reaction. The as-synthesized product was collected by filtering and washed with Milli-Q water. For comparison, the pure vanadium oxide product was obtained using the same procedure without addition of GO. Besides H_2SO_4 , various acids including HCl, HAc, and HNO_3 were utilized during fabrication to investigate the effect of the added acid on the morphology of final product.

Characterization: The morphology of the materials was investigated by field emission scanning electron microscopy (FE-SEM) using a Quanta FEG 250 Analytical ESEM, transmission electron microscopy (TEM, Tecnai T20 G2, 200 kV), and a 5500 atomic-force microscopy (AFM) system (Alignment Technology). The X-ray powder diffraction (XRD) patterns were obtained using a Huber instrument with a monochromatized Cu K α radiation of $\lambda=1.5406$ Å. Thermogravimetric analysis (TGA) was performed using a Thermogravimetric Analyzer (Mettler Toledo) to examine the weight percentage of rGO in the composite under an air atmosphere from room temperature to 700 °C with a ramping rate of 10 °C min⁻¹. UV-vis spectra were recorded on an Agilent 8453 (Santa Clara, CA) and X-ray photoelectron spectrometry (XPS) results were collected with a Thermo Scientific K-alpha spectrometer using Al K α radiation.

Electrochemical measurements: To prepare the working electrode, the steel mesh was coated by a homogenous slurry containing active material, carbon black, and PVDF in a weight ratio of 7:2:1. After that, the coated steel mesh was dried in a vacuum oven at 120 °C for 12 h. The zinc ion coin cells were assembled using active materials as the cathode, metallic zinc foil as the anode, 3 M Zn(CF₃SO₃)₂ as the electrolyte and glass microfiber filters as the separator. The mass loading (composite weight for the V₃O₇·H₂O/rGO cathode) during the testing was in a range of 0.5-1.3 mg cm⁻². Electrochemical performance of the cell was evaluated *via* an Autolab potentiostat, including galvanostatic performance at various current densities, electrochemical impedance spectroscopy (EIS) at the open-circuit voltage in a frequency range of 0.01 Hz-100 kHz, and cyclic voltammetry (CV) in a potential range of 0.2-1.6 V at a scan rate of 0.1 mV s⁻¹.

Supporting Information

Supporting Information is available from the Wiley Online Library or from the author.

Acknowledgements

The financial support from the China Scholarship Council for a Ph.D. scholarship (No. 201706220078) to H. C. and a VILLUM Experiment (grant No. 35844) to X. X. is greatly acknowledged.

Received: ((will be filled in by the editorial staff))

Revised: ((will be filled in by the editorial staff))

Published online: ((will be filled in by the editorial staff))

References

1. J. Huang; Z. Wang; M. Hou; X. Dong; Y. Liu; Y. Wang; Y. Xia, *Nat. Commun.* **2018**, *9* (1), 2906.
2. G. Fang; J. Zhou; A. Pan; S. Liang, *ACS Energy Lett.* **2018**, *3* (10), 2480-2501.
3. K. Zhao; C. Wang; Y. Yu; M. Yan; Q. Wei; P. He; Y. Dong; Z. Zhang; X. Wang; L. Mai, *Adv. Mater. Interfaces* **2018**, *5* (16), 1800848.
4. T. Wei; Q. Li; G. Yang; C. Wang, *J. Mater. Chem. A* **2018**, *6* (41), 20402-20410.
5. a) K. Lu; B. Song; Y. Zhang; H. Ma; J. Zhang, *J. Mater. Chem. A* **2017**, *5* (45), 23628-23633; b) H. Qin; Z. Yang; L. Chen; X. Chen; L. Wang, *J. Mater. Chem. A* **2018**, *6* (46), 23757-23765.
6. Y. Yang; Y. Tang; G. Fang; L. Shan; J. Guo; W. Zhang; C. Wang; L. Wang; J. Zhou; S. Liang, *Energy Environ. Sci.* **2018**, *11* (11), 3157-3162.
7. J. Ming; J. Guo; C. Xia; W. Wang; H. N. Alshareef, *Mater. Sci. Eng. R Rep* **2019**, *135*, 58-84.
8. Y. Yang; Y. Tang; S. Liang; Z. Wu; G. Fang; X. Cao; C. Wang; T. Lin; A. Pan; J. Zhou, *Nano Energy* **2019**, *61*, 617-625.
9. a) P. Jing; W. Wei; W. Luo; X. Li; F. Xu; H. Li; M. Wei; D. Yu; Q. Zhu; G. Liu, *Inorg. Chem. Commun.* **2020**, *117*, 107953; b) H. Yan; Q. Ru; P. Gao; Z. Shi; Y. Gao; F. Chen; F. Chi-Chun Ling; L. Wei, *Appl. Surf. Sci.* **2020**, *534*, 147608; c) H. Chen; L. Chen; J. Meng; Z. Yang; J. Wu; Y. Rong; L. Deng; Y. Shi, *J. Power Sources* **2020**, *474*, 228569.
10. H. Li; T. Zhai; P. He; Y. Wang; E. Hosono; H. Zhou, *J. Mater. Chem.* **2011**, *21* (6), 1780-1787.
11. W. Duan; M. Zhao; Y. Li; N. u. R. Lashari; T. Xu; F. Wang; X. Song, *Energy Fuels* **2020**, *34* (3), 3877-3886.
12. S. Gao; Z. Chen; M. Wei; K. Wei; H. Zhou, *Electrochim. Acta* **2009**, *54* (3), 1115-1118.
13. W. Huang; X. Zheng; H. Shangguan; X. Xiao; J. Tang; H. Sun; K. Mølhav; L. Ci; P. Si; J. Zhang, *Appl. Surf. Sci.* **2020**, *525*, 146513.
14. a) J. Zhong; F. Yi; A. Gao; D. Shu; Y. Huang; Z. Li; W. Zhu; C. He; T. Meng; S. Zhao, *ChemElectroChem* **2017**, *4* (5), 1088-1094; b) Z.-J. Zhang; Y.-X. Wang; S.-L. Chou; H.-J. Li; H.-K. Liu; J.-Z. Wang, *J. Power Sources* **2015**, *280*, 107-113; c) M. Darvishi; F. Jamali-Paghaleh; M. Jamali-Paghaleh; J. Seyed-Yazdi, *Surf. Interfaces* **2017**, *9*, 167-172.
15. C. M. Gilmour; C. D. K. Herd; P. Beck, *Meteorit. Planet. Sci.* **2019**, *54* (9), 1951-1972.
16. a) R. Gryboś; J. Szklarzewicz; A. Jurowska; M. Hodorowicz, *J. Mol. Struct.* **2018**, *1171*, 880-887; b) M. Le; O. Rathje; A. Levina; P. A. Lay, *JBIC J. Biol. Inorg. Chem.* **2017**, *22* (5), 663-672.
17. I. Kokal; M. Somer; P. H. L. Notten; H. T. Hintzen, *Solid State Ionics* **2011**, *185* (1), 42-46.
18. H. Cao; X. Wang; H. Gu; J. Liu; L. Luan; W. Liu; Y. Wang; Z. Guo, *RSC Adv.* **2015**, *5* (44), 34566-34571.
19. a) P. Vishnuprakash; C. Nithya; M. Premalatha, *Electrochim. Acta* **2019**, *309*, 234-241; b) G. Silversmit; D. Depla; H. Poelman; G. B. Marin; R. De Gryse, *J. Electron Spectrosc. Relat. Phenom.* **2004**, *135* (2), 167-175.
20. N. Alov; D. Kutsko; I. Spirovová; Z. Bastl, *Surf. Sci.* **2006**, *600* (8), 1628-1631.

21. C. Y. Foo; A. Sumboja; D. J. H. Tan; J. Wang; P. S. Lee, *Adv. Energy Mater.* **2014**, *4* (12), 1400236.
22. D. J. Ahirrao; K. Mohanapriya; N. Jha, *Mater. Res. Bull.* **2018**, *108*, 73-82.
23. D. Pham-Cong; K. Ahn; S. W. Hong; S. Y. Jeong; J. H. Choi; C. H. Doh; J. S. Jin; E. D. Jeong; C. R. Cho, *Curr. Appl. Phys.* **2014**, *14* (2), 215-221.
24. a) J. Lv; Q. Zhu; Z. Zeng; M. Zhang; J. Yang; M. Zhao; W. Wang; Y. Cheng; G. He; Z. Sun, *J. Phys. Chem. Solids* **2017**, *111*, 104-109; b) M. S. Abdel-wahab; A. Jilani; I. S. Yahia; A. A. Al-Ghamdi, *Superlattices Microstruct.* **2016**, *94*, 108-118.
25. T. Liu; W. Wang; M. Yi; Q. Chen; C. Xu; D. Cai; H. Zhan, *Chem. Eng. J.* **2018**, *354*, 454-462.
26. a) J. Ding; Z. Du; L. Gu; B. Li; L. Wang; S. Wang; Y. Gong; S. Yang, *Adv. Mater.* **2018**, *30* (26), 1800762; b) P. He; Y. Quan; X. Xu; M. Yan; W. Yang; Q. An; L. He; L. Mai, *Small* **2017**, *13* (47), 1702551.
27. X. Dai; F. Wan; L. Zhang; H. Cao; Z. Niu, *Energy Storage Mater.* **2019**, *17*, 143-150.
28. G. Li; Z. Yang; Y. Jiang; C. Jin; W. Huang; X. Ding; Y. Huang, *Nano Energy* **2016**, *25*, 211-217.
29. a) P. Yang; C. Feng; Y. Liu; T. Cheng; X. Yang; H. Liu; K. Liu; H. J. Fan, *Adv. Energy Mater.* **2020**, *10* (48), 2002898; b) Y. Cai; R. Chua; S. Huang; H. Ren; M. Srinivasan, *Chem. Eng. J.* **2020**, *396*, 125221; c) T. Sun; Q. Nian; S. Zheng; J. Shi; Z. Tao, *Small* **2020**, *16* (17), 2000597.
30. J. Zhou; L. Shan; Z. Wu; X. Guo; G. Fang; S. Liang, *Chem. Commun. (Cambridge, U. K.)* **2018**, *54* (35), 4457-4460.
31. H. Qin; L. Chen; L. Wang; X. Chen; Z. Yang, *Electrochim. Acta* **2019**, *306*, 307-316.
32. H. Yan; Q. Ru; P. Gao; S. Cheng; F. Chen; F. C.-C. Ling; L. Wei, *Energy Technol.* **2020**, *8* (3), 1901105.
33. J. Lai; H. Zhu; X. Zhu; H. Koritala; Y. Wang, *ACS Appl. Energy Mater.* **2019**, *2* (3), 1988-1996.
34. J. H. Jo; Y.-K. Sun; S.-T. Myung, *J. Mater. Chem. A* **2017**, *5* (18), 8367-8375.
35. Q. Pang; C. Sun; Y. Yu; K. Zhao; Z. Zhang; P. M. Voyles; G. Chen; Y. Wei; X. Wang, *Adv. Energy Mater.* **2018**, *8* (19), 1800144.
36. H.-S. Kim; J. B. Cook; H. Lin; Jesse S. Ko; Sarah H. Tolbert; V. Ozolins; B. Dunn, *Nat. Mater.* **2017**, *16* (4), 454-460.
37. Y. Liu; Z. Pan; D. Tian; T. Hu; H. Jiang; J. Yang; J. Sun; J. Zheng; C. Meng; Y. Zhang, *Chem. Eng. J.* **2020**, *399*, 125842.
38. a) S. Liu; H. Zhu; B. Zhang; G. Li; H. Zhu; Y. Ren; H. Geng; Y. Yang; Q. Liu; C. C. Li, *Adv. Mater.* **2020**, *32* (26), 2001113; b) S. Chen; K. Li; K. S. Hui; J. Zhang, *Adv. Funct. Mater.* **2020**, *30* (43), 2003890.
39. H. Geng; M. Cheng; B. Wang; Y. Yang; Y. Zhang; C. C. Li, *Adv. Funct. Mater.* **2020**, *30* (6), 1907684.
40. Y. Zhang; H. Jiang; L. Xu; Z. Gao; C. Meng, *ACS Appl. Energy Mater.* **2019**, *2* (11), 7861-7869.
41. a) C. Shen; X. Li; N. Li; K. Xie; J.-g. Wang; X. Liu; B. Wei, *ACS Appl. Mater. Interfaces* **2018**, *10* (30), 25446-25453; b) D. Chen; X. Rui; Q. Zhang; H. Geng; L. Gan; W. Zhang; C. Li; S. Huang; Y. Yu, *Nano Energy* **2019**, *60*, 171-178.
42. a) P. Hu; T. Zhu; X. Wang; X. Wei; M. Yan; J. Li; W. Luo; W. Yang; W. Zhang; L. Zhou; Z. Zhou; L. Mai, *Nano Lett.* **2018**, *18* (3), 1758-1763; b) Y. Liu; Q. Li; K. Ma; G. Yang; C. Wang, *ACS Nano* **2019**, *13* (10), 12081-12089.